

Fast photothermal spatial light modulation for quantitative phase imaging at the nanoscale

Hadrien Robert

Institute of Photonics and Electronics of the Czech Academy of Sciences <https://orcid.org/0000-0002-6185-3379>

Łukasz Bujak

Institute of Photonics and Electronics of the Czech Academy of Sciences

Kristýna Holanová

Institute of Photonics and Electronics of the Czech Academy of Sciences

Milan Vala

Institute of Photonics and Electronics of the Czech Academy of Sciences <https://orcid.org/0000-0003-4958-1750>

Piliarik Marek (✉ piliarik@ufe.cz)

Institute of Photonics and Electronics of the Czech Academy of Sciences <https://orcid.org/0000-0002-2567-551X>

Article

Keywords: Spatial light modulator, thermoplasmonic, interferometric microscopy, quantitative phase imaging, microtubules

Posted Date: July 12th, 2020

DOI: <https://doi.org/10.21203/rs.3.rs-38429/v1>

License:  This work is licensed under a Creative Commons Attribution 4.0 International License.

[Read Full License](#)

Version of Record: A version of this preprint was published at Nature Communications on May 19th, 2021. See the published version at <https://doi.org/10.1038/s41467-021-23252-3>.

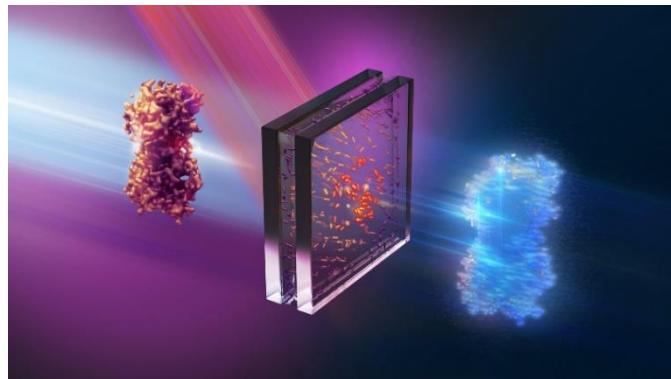
Fast photothermal spatial light modulation for quantitative phase imaging at the nanoscale

*Hadrien M.L. Robert, Łukasz Bujak, Kristýna Holanová, Milan Vala and Marek Piliarik**

Institute of Photonics and Electronics of the Czech Academy of Sciences, Chaberská 1014/57,
18251 Prague, Czech Republic.

E-mail: piliarik@ufe.cz,

Keywords: Spatial light modulator, thermoplasmonic, interferometric microscopy, quantitative phase imaging, microtubules.



Abstract

Spatial light modulators have become an essential tool for advanced microscopy enabling breakthroughs in 3D, phase, or super-resolution imaging. However, continuous spatial-light modulation without diffraction artifacts, polarization dependence, and able to capture sub-ms microscopic motion is challenging. Here we present a photothermal spatial light modulator (PT-SLM) enabling the fast wavefront shaping free of diffraction artifacts, having a high transmissivity and modulation efficiency independent of light polarization. It is based on the microscopic heating of a thin layer of thermo-optic material confined between the photothermal heat-source and a

transparent heatsink. We achieve a phase-shift $> \pi$ with a response time as short as 70 μs with a theoretical limit in the sub- μs range. The combination of the PT-SLM with an interferometric scattering microscope (iSCAT) allowed us to perform quantitative phase imaging of sub-diffractive scatterers and decipher the 3D nanoscopic displacement of microtubules matching closely with control data from atomic force microscopy.

Interferometric microscopes employ interference between at least two light waves, usually a reference and a probe wave, to get information about microscopic objects. Numerous methods based on this principle have been developed, including the phase-contrast microscope,¹ the holographic microscope,² the Nomarski microscope,³ or the interferometric reflection microscope.⁴ Additionally, by shaping the reference wave, the phase profile of the probe wavefront can be reconstructed.⁵ This approach, established as quantitative phase imaging (QPI), became a powerful tool for capturing phase images of transparent samples in transmission including single cells⁶ or mapping the phase of opaque structures in a reflection configuration.⁷ Besides specific applications in plasmonic imaging,^{8,9} QPI of weak scatterers remains complex to achieve. Recently, interferometric scattering microscopy (iSCAT) has become the method of choice for ultrasensitive imaging and localization of sub-wavelength scatterers including unlabeled single proteins with a high spatiotemporal resolution.¹⁰⁻¹² In the iSCAT microscope, the light wave scattered on the sample and the reference wave reflected from the sample substrate share a simple imaging path and interfere on a detector. However, any direct control of the phase-shift in iSCAT microscopy is challenging due to its strong sensitivity to small wavefront distortion.¹³ There are several modern techniques for wavefront shaping including deformable mirrors, micromirror devices, or liquid crystal spatial light modulators (LC-SLMs).¹⁴⁻¹⁶ LC-SLMs have

become the central tool for beam shaping in microscopy featuring high resolution (few μm) and high definition (several millions of pixels) at affordable prices. However, due to their intrinsic properties, wave-shaping using LC-SLMs has never been successfully implemented in an ultrasensitive iSCAT setup. LC-SLMs have limited phase stability, are polarization-sensitive, suffer from strong diffractive effects, and have an intrinsic response time of several ms. To enhance the phase modulation speed to kHz range, technologies such as ferroelectric LC-SLMs and micromirror devices are used at the cost of the diffraction efficiency and the possibility of only discrete (usually on-off) modulation.¹⁵

To overcome these limitations, spatial-light modulators based on thermo-optics effects have been recently introduced. The thermo-optic modulation is well established in guided wave optics via plasmonic modulators^{17,18} and with active metasurfaces for mid/far-infrared wavelengths.^{19,20} It has been employed to visible and free-space optics in combination with thermoplasmonics means,²¹ to perform thermal imaging,²² measure temperature gradients,^{23,24} generate adjustable thermal lenses,²⁵ or shape temperature profiles with a modulated light wave.^{26,27} Most recently, there has been a focused research effort to generalize thermally driven wavefront shaping, e.g., by the combined effect of photo-thermal lenses with remaining challenges in speed and lateral resolution.²⁸⁻³⁰

Here, we introduce a photothermal spatial light modulator (PT-SLM) enabling the adjustment of the phase-shift between the scattered light and the reference beam in iSCAT microscopy. We implement the new technology for quantitative phase imaging by placing the PT-SLM in a Fourier plane of an iSCAT microscope and extract the full phase information of the light scattered on weak scatterers. We characterize the 3D phase profiles of light scattered on sub-wavelength scatterers and demonstrate the 3D reconstruction of biological nanostructures.

Results

PT-SLM principle and numerical simulations. The PT-SLM relies on microscopic heating of a layer of thermo-optic material whose refractive index is highly sensitive to temperature. To achieve locally restricted heating, we use the photothermal effect in a layer of gold nanorods patterned on a surface.²¹ We introduce the concept of confining the generated temperature change within the desired area by only optimizing the heat gradients and dissipation rates. The structure of the device is depicted in **Figure 1a**. Incident plane waves illuminate a layered structure made of a glass BK7 substrate, a thin layer of thermo-optic material, i.e., liquid glycerol, and a transparent heat sink superstrate made of sapphire. In essence, the heat generated on one side of the thermo-optic material builds a laterally uniform temperature gradient across the layer of the thermo-optic material and dissipates into the transparent heat sink. The temperature change within the thermo-optic material varies its refractive index resulting in phase retardation of the transmitted optical wave.

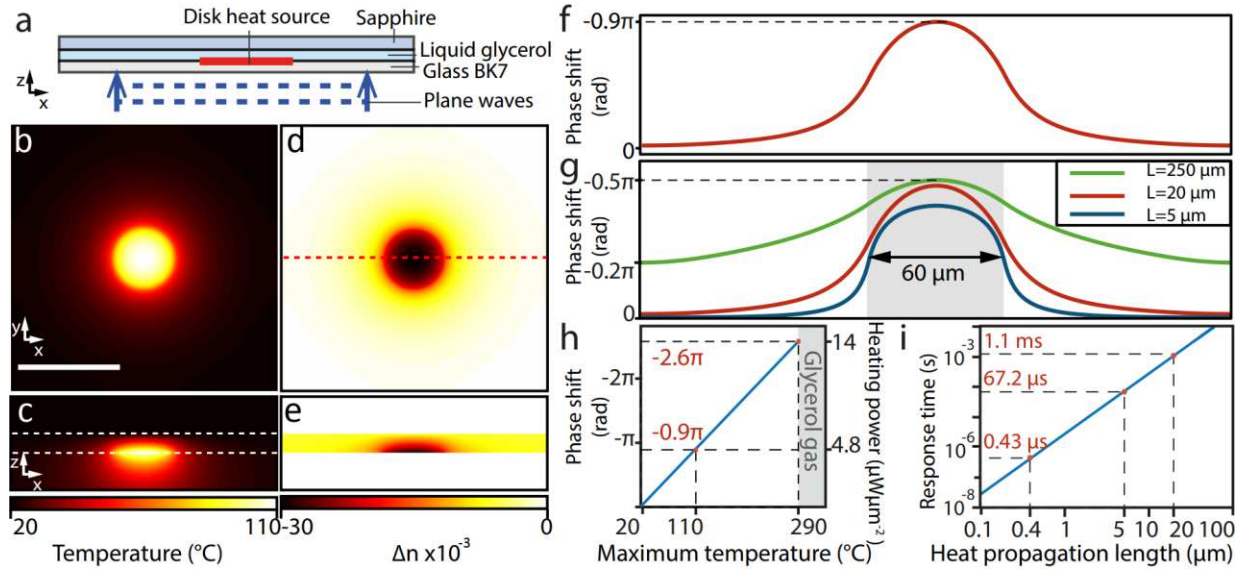


Figure 1. Numerical simulation of the spatial phase modulator. a) Illustration of the structure used. b) 2D map of temperature in the xy cross-section and c) xz cross-section (scale bar=100 μm). The boundaries of the thermo-optic material are indicated by the two white dashed lines. d) Resulting refractive index variation in the xy cross-section, and e) in the xz cross-section. f) Phase-shift profile of a plane wave propagating through the structure in z at the position of the red dashed line in d). g) Phase-shift profiles for different thicknesses of the thermo-optic layer. Heating powers of $0.4 \mu\text{W}\mu\text{m}^{-2}$, $2.6 \mu\text{W}\mu\text{m}^{-2}$, and $14 \mu\text{W}\mu\text{m}^{-2}$ were considered for thicknesses of 250 μm , 20 μm , and 5 μm respectively. h) Peak phase-shift and corresponding heating power as a function of the peak temperature change (glycerol thickness=20 μm). i) Response time of the temperature change as a function of the characteristic dimension according to the model.

To study the effect of a microscopic heat source on the optical phase of incoming light, we use a theoretical model solving the static heat equation in a three-layered system³¹ (detailed in Supplementary information section S1). The geometry of the numerical model is shown in Figure 1a. We model a heat source of a fixed diameter of 60 μm delivering a heating power of $Q=4.8$

$\mu\text{W}\mu\text{m}^{-2}$ interfaced with a 20- μm -thick layer of thermo-optic material (glycerol considered in the model). Figure 1b-c depicts the 3D temperature profile induced by the heat source in a steady-state, and the resulting 3D distribution of the refractive index is shown in Figure 1d-e. We observe that the refractive index gradient is confined within the thermo-optic material. This confinement is due to the thermo-optic coefficient, $\Delta n/\Delta T$, of glycerol, which exceeds the one of glass by a factor of >10 . The resulting phase-shift cross-section of normally-incident plane waves ($\lambda=488$ nm) transmitted through the structure is shown in Figure 1f. In the model, the phase-shift peaks at 0.9π in the center of the heated area and drops rapidly outside the heat source. The strong thermal gradient around the heat source is explained by the thermal conductivity of the superstrate, which is more than 100-times higher for sapphire than for glycerol (details in Supplementary Figure S2). The effect of the thickness of the thermo-optic material layer is shown in Figure 1g. Clearly, decreasing the thickness results in a phase-shift profile more confined to the area of the heat source, and a more uniform phase-shift profile within the heated area. Indeed, the lateral distribution of the phase shift around the edge of a heat source is limited by the temperature gradient generated in the layer of thermo-optic material, and consequently by the thickness of the layer. The peak phase-shift scales linearly with the maximum temperature until reaching the boiling temperature of glycerol as shown in Figure 1h, which corresponds to a maximum phase-shift of 2.6π . Supplementary Figure S3 shows that this maximum can be increased with the thickness of the glycerol layer.

The characteristic response time τ of a thermal process to be in a steady-state is estimated from the heat equation and is expressed as, $\tau = L^2/4D$, where L is a characteristic size of the system, e.g., the thermo-optic layer thickness, or the heated area diameter depending on which parameter limits the heat propagation, and D is the medium thermal diffusivity.³² Considering the glycerol

thickness of $L=20\ \mu\text{m}$ and the thermal diffusivity of $D=0.096\ \text{mm}^2\text{s}^{-1}$, the response time yields $\tau=1.1\ \text{ms}$. The dependence of the response time is shown in Figure 1i. The reduction of the glycerol layer thickness to $5\ \mu\text{m}$ decreases the response time to $67.2\ \mu\text{s}$. We estimate a minimum achievable response time of $430\ \text{ns}$ corresponding to the smallest optically addressable area, which is limited by the diffraction limit ($\sim 400\ \text{nm}$).

Implementation of the PT-SLM. We prototyped a PT-SLM and combined it with an iSCAT microscope. To generate the disk-shaped heat source, we used the photothermal effect of a layer of gold nanorods. Gold nanorods with average size of $20\ \text{nm} \times 50\ \text{nm}$ were immobilized on a glass coverslip to obtain homogeneous spatial distribution and random orientation. The average surface density of gold nanorods was $300\ \mu\text{m}^{-2}$ with less than 20% variation (Supplementary Figure S4a). A $20\text{-}\mu\text{m}$ -thick layer of liquid glycerol was sandwiched between the glass coverslip and a sapphire window with the layer of gold nanorods at the glass/glycerol interface. A continuous laser light source ($\lambda=660\ \text{nm}$), providing a heating beam modulated via an acousto-optic modulator, was focused on the surface of the nanorods into a spot of uniform illumination of $60\ \mu\text{m}$ in diameter (inset **Figure 2a**). The surface density of nanorods is sufficiently high to be considered as a homogeneous heat source equivalent to the area of the heating beam.³³ The extinction rate of the layer of nanorods was 13.6% at 660 nm (Figure S4b). To generate a peak heating power of $4.8\ \mu\text{W}\mu\text{m}^{-2}$ within the illuminated surface of $60\text{-}\mu\text{m}$ diameter, we used an incoming light power of 100 mW.

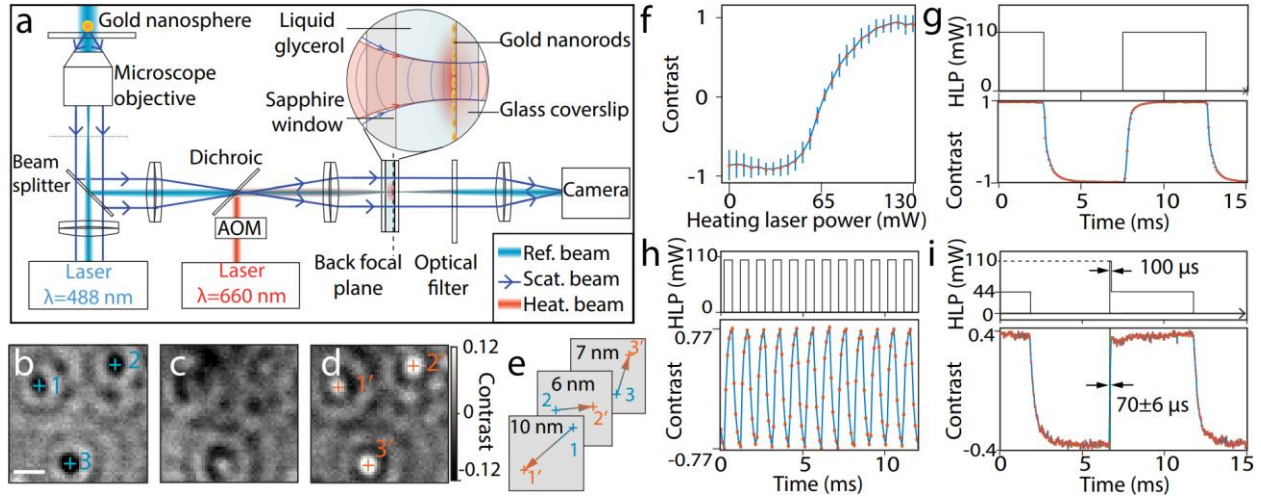


Figure 2. Experimental characterization of the PT-SLM. a) Layout of the setup (not to scale), details of the phase modulator structure are magnified. b-d) Normalized iSCAT images of 30-nm single gold nanospheres at heating laser powers P_{heat} (total power incident on the modulator structure) of b) 0 mW, c) 65 mW, d) 110 mW. (Scale bar=500 nm). Blue and orange crosses and numbers indicate the positions used to assess the lateral distortion. e) Change in the fitted position of the three nanoparticles indicated in b) and d). f) Calibration curve of the particle contrast dependence on the heating power. Error bars indicate the standard deviation of the experiment. g) Time series of the contrast of a gold nanosphere modulated with a rectangular signal at 100 Hz (HLP = Heating Laser Power) and h) at 1 kHz. i) Contrast time series for an arbitrary-shaped heating modulation. The upper diagram shows the corresponding temporal profile of the heating beam intensity.

The iSCAT setup is sketched in Figure 2a. A test sample of 30-nm gold nanospheres spin-coated on a glass coverslip is illuminated by a collimated imaging beam (continuous laser, $\lambda=488$ nm) through a microscope objective. The imaging beam is partially reflected at the coverslip surface

and partially scattered on the sample. Both scattered and reflected beams are collected by the microscope objective and routed via a beam splitter through a 4f system with the thermo-optic modulator system at the common focus to be imaged on a CMOS camera.

The intensity of light I_d detected by the camera is the sum of the light intensities of the scattered beam and the reference beam and the cross term representing beating between the waves as $I_d = I_{inc}(r^2 + s^2 + 2rs \cos(\Delta\varphi))$, where I_{inc} is the incoming irradiance (Wm^{-2}), r is the coverslip amplitude reflectivity, s is the scattering amplitude, and $\Delta\varphi$ is the phase difference between the scattered and reference waves. As $s^2 \ll r^2$, the contrast C of the interference image is expressed as:¹⁰

$$C = 2(s/r) \cos \Delta\varphi. (1)$$

Considering a nanoparticle at a distance z from the coverslip and surrounded by a medium with a refractive index n , the term $\Delta\varphi$ is defined as $\Delta\varphi = \frac{4\pi}{\lambda}nz + \varphi_{Gouy} + \varphi_{scat}$, where φ_{Gouy} is the Gouy phase due to the focus position and φ_{scat} is the phase of the polarizability of the nanoparticle. The image contrast is, therefore, determined by the nanoparticle distance from the surface and the Gouy phase due to a change in the focus position. Thus, for a static nanoparticle, a change in the phase of the reference beam results in a contrast variation of the interferometric image. To adjust the phase of the reference beam, we spatially overlap the Gaussian profile of the reference beam (approximate diameter at half maximum of 30 μm) with the heating beam in the central region of the thermo-optic modulator. The scattered beam propagates through the thermo-optic modulator approximately collimated with the beam diameter of 1.2 mm. The fraction of the scattered beam influenced by the heating beam is therefore as small as 0.25%, which can be considered as negligible compared to a typical signal-to-noise ratio of a single scatterer image, i.e., around 40

for 20-nm gold nanospheres.³⁴ Measured transmissivity of the PT-SLM was 82% at the wavelength of 488 nm.

Figure 2b shows a typical image of nanospheres (diameter=30 nm) in the interferometric microscope without additional phase-shift modulation. The image contrast was first set by fine adjustment of the focal position without applying any phase modulation. Figure 2c-d shows the effect of increasing the heating laser power to 60 mW and 110 mW, respectively. The dependence of the contrast of the nanospheres image on the light intensity of the heating beam is shown in Figure 2f (raw data are shown in Supplementary Figure S5). To change the phase delay between the interfering beams by π , an absolute change in the light intensity of the heating beam by 70 mW was required, which is equivalent to a delivered heat of about $Q=3.4 \mu\text{W}\mu\text{m}^{-2}$. This observation approximately agrees with the estimation derived from the theoretical model ($Q=4.8 \mu\text{W}\mu\text{m}^{-2}$).

We characterized the distortion of the interferometric image of the scattered wave associated with the thermo-induced phase-shift of the reference wave. We used a 2D Gaussian fit to estimate the positions of the interferometric minima (corresponding to the heating power of 40 mW) and the interferometric maxima (corresponding to the heating power of 110 mW). By comparing the absolute change in the estimated positions of the images of three different nanospheres, we found that shifting the phase of the reference beam by π distorts the image by less than 10 nm in all directions (Figure 2e). The distortion is thus less than 0.5% of the field of view, allowing to adjust the contrast of a scattering object (e.g., a label) and follow its position in three dimensions without compromising the lateral localization fidelity.

Figure 2g illustrates the temporal change of the image contrast in response to a 100 Hz square modulation. The phase change requires up to 1 ms until it reaches 96% of the steady-state level (rising time= 0.94 ± 0.2 ms and falling time= 1.0 ± 0.2 ms), which is consistent with the theoretical

model in Figure 1i. The maximum rate of the phase change is limited by the heat propagation through the glycerol layer yielding 10 ± 2 mrad μs^{-1} . It is worth noting that the temporal evolution of the contrast is not a single-exponential function due to different rates of heat dissipation in the materials of the phase modulator structure. Therefore, even at 1 kHz phase modulation, we were able to achieve 77% of the maximum phase modulation, Figure 2h. To exploit the maximum rate of the phase change offered by the geometry of the PT-SLM, we optimized the temporal profile of the heating intensity as shown in Figure 2h. The temporal heat profile begins with a 100- μs pulse with a heating laser power of 110 mW. It is followed by a sharp decrease in the heating laser power (44 mW) to stabilize the temperature increase towards a steady state. Based on the analysis of 100 modulation cycles, we achieved the mean rise time of 0.3π phase switching as short as 70 ± 6 μs (defined here as 20% to 80% of the magnitude of the signal).

Quantitative phase imaging of nanoscatterers. Having direct control of the interference contrast with the PT-SLM, we developed a method of quantitative phase imaging of light scattered by nanoscopic scatterers. We collect a series of images of a single scatterer while modulating the phase-shift of the reference wave, and extract the terms s/r and $\Delta\varphi$ from contrast variation using least-square fitting of Equation (1) (details in Supplementary Information S6). Figure 3a-c depict images of two gold nanospheres (30 nm) at different focus positions and calculated squared amplitude $(s/r)^2$ and a phase image. Figure 3d plots the variation of the extracted phase of both nanoparticles as a function of the focus displacement over 1.5 μm . The phase profile corresponds to the Gouy phase of a focused coherent optical beam which is known to follow arctangent function for a Gaussian beam; however, in the image of an optical microscope follows a linear dependence on the focus position.³⁵ The theoretical Gouy phase profile closely matches experimental data as

shown in Figure 3d following the dependence $d\phi_{\text{Gouy}}/dz = ka^2/4f^2$, with $k=2\pi/\lambda$ the wavenumber, a is the radius of the aperture and f the focal length of the microscope objective.

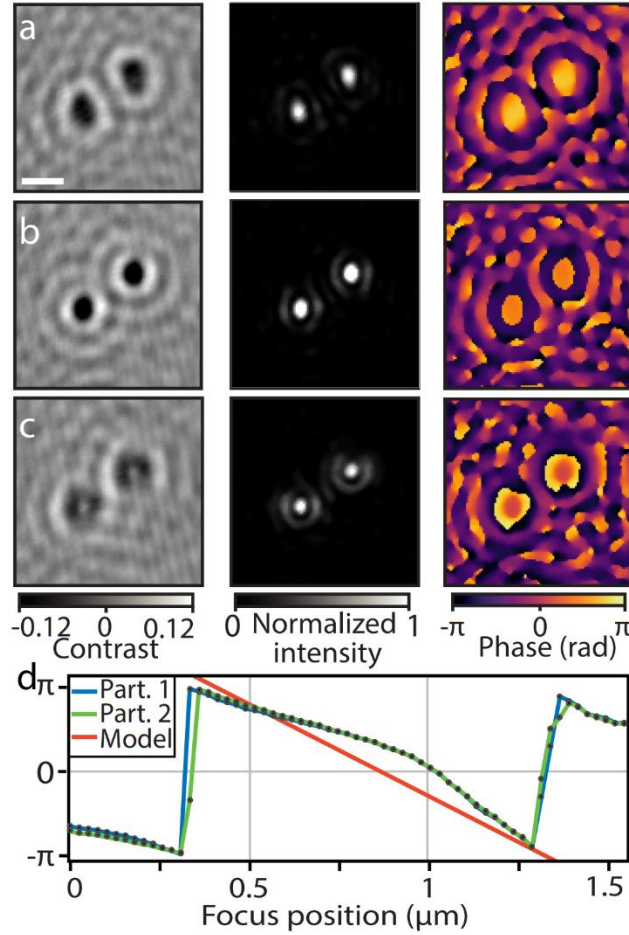


Figure 3. Quantitative phase imaging of gold nanoparticles. a-c) From left to right: iSCAT contrast, reconstructed intensity, and phase image of two gold nanoparticles at the focus positions: a) 0.35 μm , b) 0.6 μm and c) 0.85 μm . Scale bar 500 nm. d) Focus position dependence of the phase for the two particles shown in a-c). A theoretical prediction is shown in red.

To demonstrate the usability of the nanoscopic QPI method for biological nanostructures, we imaged two microtubules, shown in Figure 4a, overlapping on an atomically flat mica surface

supported by a coverslip¹². The specific geometry of the sample allowed us to separate the images of the two microtubules, by subtracting the fringe pattern generated by each of the microtubules outside of the crossing region as shown in Figure 4b-c (details in Supplementary Information S7). The local fluctuation of the microtubule scattering phase indicates changes in the distance z between the microtubule and the surface. We extract the vertical coordinate of the microtubule scattering as $z = \frac{\lambda}{4\pi n} \Delta\varphi$ and reconstruct a 3D profiles of microtubule crossing in ribbon-like surfaces in Figure 3h. The height profiles indicate that one of the microtubules, the green ribbon corresponding to Figure 4d, features a vertical displacement at the location of the microtubule crossing peaking at 40 nm with a full width of 500 nm which is larger than the microscope point-spread function. We carried out a control experiment using an atomic force microscope of an equivalent microtubule structure shown in Figure 4e. The control experiment shows a strikingly similar geometry of the microtubule crossing (36 nm displacement peak of 500 nm width). A more detailed analysis of the shape corrugation of a microtubule attached to the surface using different densities of kinesin linkers is described in Supplementary Information S8.

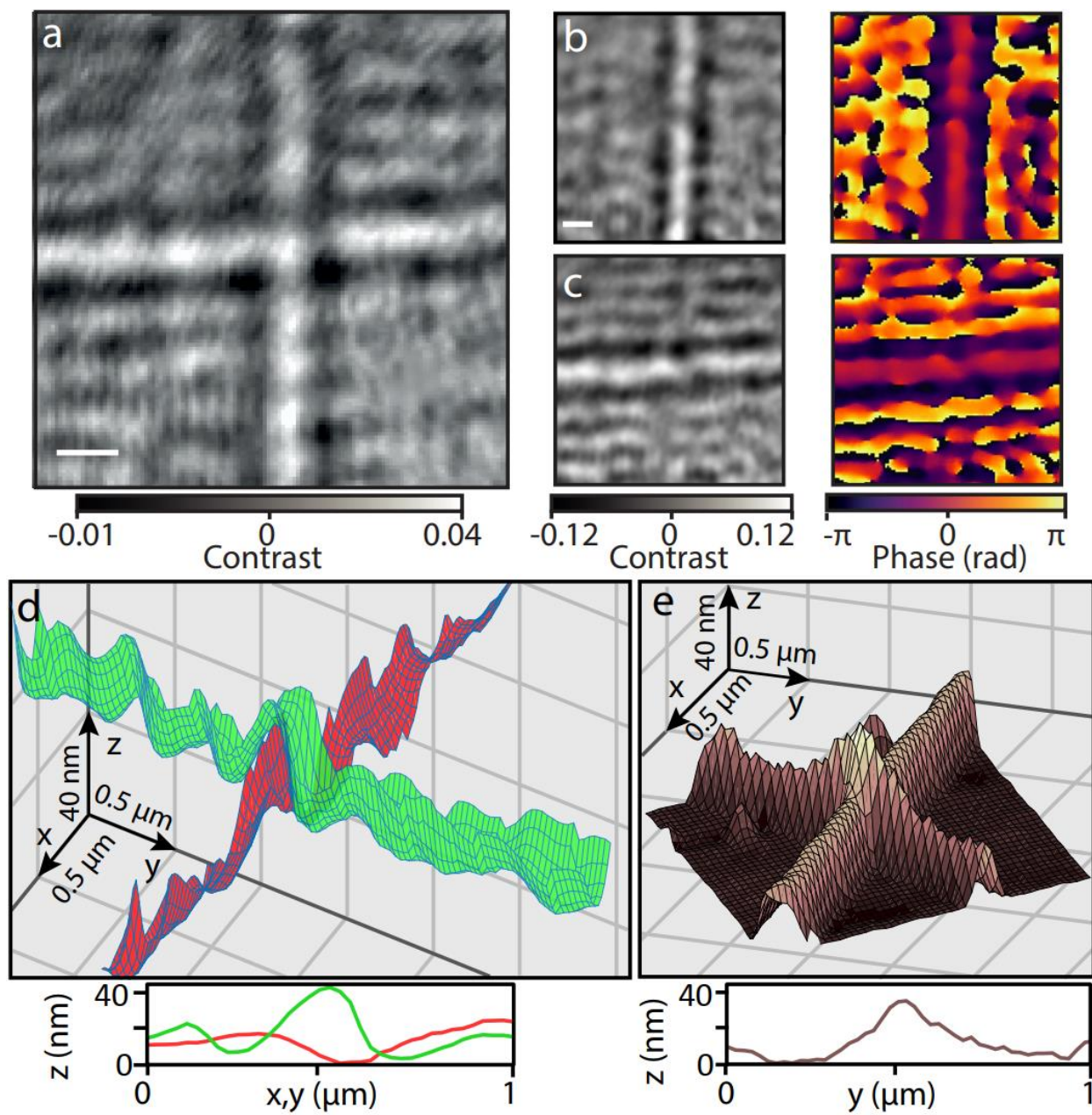


Figure 4. Quantitative phase imaging of microtubules. a) iSCAT image of two microtubules. Scale bar 500 nm. b-c) Separated iSCAT images and phase images of individual microtubules shown in a). d) 3D reconstruction of the crossing microtubules and the cross-section height profile. e) AFM image of microtubule crossing and the corresponding height profile.

Discussion

We demonstrated a new concept of spatially resolved optical phase modulation based on the photothermally driven thermo-optic effect enabling the fast and highly spatially confined phase adjustment of a free-space optical beam. We combined the PT-SLM with an interferometric scattering microscope to specifically address the reference arm of the common-path interferometer and performed quantitative phase imaging with exceptional nanoscopic sensitivity. It is worth mentioning that iSCAT imaging is highly sensitive to any wavefront perturbation. To date, any wavefront shaping involving LC-SLM failed in integration with iSCAT due to phase stability and diffraction speckles. The PT-SLM presented here is proved compatible with the most demanding iSCAT applications as modulations occur exclusively at the lowest spatial frequencies of the scattering beam (0.25% of the beam area), it works in transmission, and suffers from no grating or polarization effect. In our proof of concept experiment, we achieved the switching time of the phase as fast as 70 μs , which is by two orders of magnitude faster than conventional LC-SLM devices and one order of magnitude faster than previously reported thermo-optic spatial-light modulation techniques.³⁰ We argue, that thanks to this unique concept of the photothermal phase modulator featuring a marginal distortion of the optical image of less than 0.5% (10 nm), we could efficiently extract the scattering phase information. Besides, we demonstrated the sensitivity of the nanoscopic QPI to accurately characterize the scattering phase of single gold nanoparticles and managed to obtain a 3D map of single microtubules crossing. This new level of performance pushes the limits of the QPI deep into the sub-diffractive regime and opens new horizons in wave-shaping. Indeed, there are numerous other applications foreseen to exploit the potential of this PT-SLM technique, ranging from microscopy, biomedical imaging, or digital holography, to astronomy.

Methods

Simulation parameters. For the presented simulations Figure 1, we considered a disk heat source with a diameter of 60 μm , delivering heating power ranging from 0.4 to 14 $\mu\text{W}\mu\text{m}^{-1}$, a glycerol thickness $L=5, 20$ and $250 \mu\text{m}$ with a thermal conductivity $\kappa=0.285 \text{ Wm}^{-1}\text{K}^{-1}$, a 140 μm thick glass BK7 layer with $\kappa=1.2 \text{ Wm}^{-1}\text{K}^{-1}$ and a 140 μm sapphire layer with $\kappa=27.21 \text{ Wm}^{-1}\text{K}^{-1}$. To calculate the refractive index variation of glycerol, we use the first order of Taylor expansion coefficient: for glycerol $\Delta n/\Delta T=-2.7 \times 10^{-4} \text{ K}^{-1}$, for BK7 glass $\Delta n/\Delta T=3 \times 10^{-6} \text{ K}^{-1}$ and sapphire $\Delta n/\Delta T=13 \times 10^{-6} \text{ K}^{-1}$. Simulations were processed with the Matlab software.

Photothermal layer preparation. The gold nanorods synthesis is adapted from the protocols developed by Nikoobakht et al.³⁶ and Liu et al.³⁷, and detailed in previous work.³⁸ The gold nanorods were functionalized with PVP. A cleaned glass coverslip has been functionalized by deposition of 3 layers of polyelectrolytes as described in the work of Vial et al.³⁹ The functionalized coverslips were immersed in a solution of PVP gold nanorods for 3 hours. The deposition was promoted via electrostatic interactions between the positively charged coverslip and the negatively charged gold nanorods.

To confine the liquid glycerol thickness, we deposited 10 μL of glycerol on the photothermal layer and sandwiched the drop with a sapphire window. The thickness of the glycerol layer was estimated from the area wetted by the glycerol layer, yielding approximately 20 μm .

Sample preparation. Coverslips were washed in ethanol and cleaned using a plasma cleaner (Zepto-BLS, Electronic Diener). The 30 nm gold nanospheres (BBI Solutions) were directly spin-coated on a glass coverslip. For the crossed microtubule experiments (iSCAT and AFM), we

immobilized microtubules stabilized with GMPCPP (a non-hydrolyzable analog of GTP) and Taxol⁴⁰ to a positively charged surface of mica glued to the glass coverslip.¹² We flowed the microtubule solution through an X-shaped flow chamber consecutively at the two perpendicular flow directions.

Optical setup specification. The imaging light source used in the iSCAT experiment was a continuous laser iBeam smart, TOPTICA Photonics AG, $\lambda=488$ nm. A microscope objective α Plan-Apochroma Zeiss x100, NA=1.46 was used to image the sample on a CMOS-based camera from Photon focus, MV1-1024E-160-CL at a total magnification of x333. The heating light source used was a continuous laser Cobolt Flamenco, $\lambda=660$ nm modulated with an acousto-optic modulator from AA Opto-Electronic, MT90-A1 vis. A piezo stage was used to manipulate the sample.

AFM characterization of microtubules. The morphology of the microtubules immobilized on the glass surface was measured using an atomic force microscope NanoWizard3 (JPK instruments AG). A special cuvette with a glass coverslip bottom functionalized with poly-L-ornithine was filled with BRB80 buffer followed by injection of GMPCPP microtubules using a micropipette. A force spectroscopy mode (QITM mode) of the AFM and qp-Bio AC cantilevers (Nanosensors, Switzerland) were used to probe the crossed MTs with force constant setpoint down to 0.1 N/m to prevent mechanical damage of the MT.

Image acquisition and data processing. To discern the scattering of the investigated specimen, all images were normalized to the illumination pattern for each focus position and each heating

power. The reference illumination pattern was averaged from raw images acquired while the sample was moved circularly with a diameter of 5 μm . To characterize the residual image distortion the apparent image positions of nanoparticles were localized by 2D Gaussian fitting using an ImageJ plugin TrackMate⁴¹. Amplitude and phase images were calculated using the Matlab software.

Acknowledgments

This work was funded by the Ministry of Education, Youth and Sports of the Czech Republic under the project LL1602 and by the Czech Science Foundation under the project 18-19705S. The authors thank Guillaume Baffou, Nicholas Scott Lynn, and Xavier Audier for scientific discussions.

Author contribution

H.M.L.R. and M.P. conceived the research, H.M.L.R. derived the theory, carried out the experiments, processed and interpreted the data, L.B. developed the experiment control and acquisition software, K.H. developed the microtubule assay, M.V. carried out the AFM study, H.M.L.R. and MP wrote the manuscript.

Competing interests

The authors declare the following competing interests: H.M.L.R. and M.P. of the Institute of Photonics and Electronics CAS have filed a patent application related to the method of phase modulation.

Additional Information

Supplementary Information is available for this paper at ...

References

1. Zernike, F. Phase contrast, a new method for the microscopic observation of transparent objects part II. *Physica* **9**, 974–986 (1942).
2. Ellis, G. W. Holomicrography: transformation of image during reconstruction of a posteriori. *Science* **154**, 1195–7 (1966).
3. G Nomarski. Nouveau dispositif pour l'observation en contraste de phase différentiel. *J. Phys. Radium* **16**, S88–S8, (1955).
4. Curtis, A. S. The mechanism of adhesion of cells to glass. A study by interference reflection microscopy. *J. Cell Biol.* **20**, 199–215 (1964).
5. Wolf, E. *Progress in optics. Volume 57*. (Elsevier, 2012).
6. Park, Y. K., Depeursinge, C. & Popescu, G. Quantitative phase imaging in biomedicine. *Nature Photonics* **12**, 578–589 (2018).
7. Kandel, M. E. *et al.* Epi-illumination gradient light interference microscopy for imaging opaque structures. *Nat. Commun.* **10**, 1–9 (2019).
8. Yang, Y., Zhai, C., Zeng, Q., Khan, A. L. & Yu, H. Quantitative Amplitude and Phase Imaging with Interferometric Plasmonic Microscopy. *ACS Nano* **13**, 13595–13601 (2019).
9. Bouchal, P. *et al.* High-Resolution Quantitative Phase Imaging of Plasmonic Metasurfaces with Sensitivity down to a Single Nanoantenna. *Nano Lett.* **19**, 1242–1250 (2019).
10. Lindfors, K., Kalkbrenner, T., Stoller, P. & Sandoghdar, V. Detection and Spectroscopy of Gold Nanoparticles Using Supercontinuum White Light Confocal Microscopy. *Phys. Rev.*

- Lett.* **93**, 037401 (2004).
11. Piliarik, M. & Sandoghdar, V. Direct optical sensing of single unlabelled proteins and super-resolution imaging of their binding sites. *Nat. Commun.* **5**, 4495 (2014).
 12. Holanová, K., Vala, M. & Piliarik, M. Optical imaging and localization of prospective scattering labels smaller than a single protein. *Opt. Laser Technol.* **109**, 323–327 (2019).
 13. Taylor, R. W. *et al.* Interferometric scattering microscopy reveals microsecond nanoscopic protein motion on a live cell membrane. *Nat. Photonics* **13**, 480–487 (2019).
 14. Gad-el-Hak, M. *The MEMS Handbook. Mechanics of Composite Materials* **23**, (2001).
 15. Maurer, C., Jesacher, A., Bernet, S. & Ritsch-Marte, M. What spatial light modulators can do for optical microscopy. *Laser Photon. Rev.* **5**, 81–101 (2011).
 16. Rubinsztein-Dunlop, H. *et al.* Roadmap on structured light. *J. Opt.* **19**, 013001 (2017).
 17. Nikolajsen, T., Leosson, K. & Bozhevolnyi, S. I. Surface plasmon polariton based modulators and switches operating at telecom wavelengths. *Appl. Phys. Lett.* **85**, 5833–5835 (2004).
 18. Mattiussi, G. A., Gagnon, G., Lahoud, N. & Berini, P. Thermally Activated Variable Attenuation of Long-Range Surface Plasmon-Polariton Waves. *J. Light. Technol.* **24**, 4391–4402 (2006).
 19. Park, J., Kang, J.-H., Kim, S. J., Liu, X. & Brongersma, M. L. Dynamic Reflection Phase and Polarization Control in Metasurfaces. *Nano Lett.* **17**, 407–413 (2017).
 20. Sherrott, M. C. *et al.* Experimental Demonstration of 230° Phase Modulation in Gate-Tunable Graphene–Gold Reconfigurable Mid-Infrared Metasurfaces. *Nano Lett.* **17**, 3027–3034 (2017).
 21. Baffou, G. & Quidant, R. Thermo-plasmonics: using metallic nanostructures as nano-

- sources of heat. *Laser Photon. Rev.* **7**, 171–187 (2013).
22. Boyer, D., Tamarat, P., Maali, A., Lounis, B. & Orrit, M. Photothermal imaging of nanometer-sized metal particles among scatterers. *Science* **297**, 1160–3 (2002).
 23. Bon, P., Maucort, G., Wattellier, B. & Monneret, S. Quadriwave lateral shearing interferometry for quantitative phase microscopy of living cells. *Opt. Express* **17**, 13080–13094 (2009).
 24. Robert, H. M. L. *et al.* Light-Assisted Solvothermal Chemistry Using Plasmonic Nanoparticles. *ACS Omega* **1**, 2–8 (2016).
 25. Donner, J. S., Morales-Dalmau, J., Alda, I., Marty, R. & Quidant, R. Fast and Transparent Adaptive Lens Based on Plasmonic Heating. *ACS Photonics* **2**, 355–360 (2015).
 26. Durdevic, L., Robert, H. M. L., Wattellier, B., Monneret, S. & Baffou, G. Microscale Temperature Shaping Using Spatial Light Modulation on Gold Nanoparticles. *Sci. Rep.* **9**, 4644 (2019).
 27. Liu, C., Tessier, G., Flores Esparza, S. I., Guillon, M. & Berto, P. Reconfigurable Temperature Control at the Microscale by Light Shaping. *ACS Photonics* **6**, 422–428 (2019).
 28. Zhang, W., Zappe, H. & Seifert, A. Wafer-scale fabricated thermo-pneumatically tunable microlenses. *Light Sci. Appl.* **3**, e145–e145 (2014).
 29. Angelini, A., Pirani, F., Frascella, F. & Descrovi, E. Reconfigurable elastomeric graded-index optical elements controlled by light. *Light Sci. Appl.* **7**, 7 (2018).
 30. Berto, P. *et al.* Tunable and free-form planar optics. *Nat. Photonics* **13**, 649–656 (2019).
 31. Ramanan, V. S., Muthukumar, M., Gnanasekaran, S., Reddy, M. J. V. & Emmanuel, B. Green's functions for the Laplace equation in a 3-layer medium, boundary element integrals

- and their application to cathodic protection. *Eng. Anal. Bound. Elem.* **23**, 777–786 (1999).
32. Berto, P., Mohamed, M. S. A., Rigneault, H. & Baffou, G. Time-harmonic optical heating of plasmonic nanoparticles. *Phys. Rev. B* **90**, 035439 (2014).
 33. Baffou, G. *et al.* Photoinduced heating of nanoparticle arrays. *ACS Nano* **7**, 6478–6488 (2013).
 34. Lin, Y.-H., Chang, W.-L. & Hsieh, C.-L. Shot-noise limited localization of single 20 nm gold particles with nanometer spatial precision within microseconds. *Opt. Express* **22**, 9159 (2014).
 35. Pang, X., Fischer, D. G. & Visser, T. D. Generalized Gouy phase for focused partially coherent light and its implications for interferometry. *J. Opt. Soc. Am. A* **29**, 989 (2012).
 36. Nikoobakht, B. & El-Sayed, M. A. Preparation and growth mechanism of gold nanorods (NRs) using seed-mediated growth method. *Chem. Mater* **15**, 1957–1962 (2003).
 37. Liu, M. & Guyot-Sionnest, P. Synthesis and optical characterization of Au/Ag core/shell nanorods. *J. Phys. Chem. B* **108**, 5882–5888 (2004).
 38. Robert, H. M. L. *et al.* Photothermal Control of Heat-Shock Protein Expression at the Single Cell Level. *Small* **14**, 1801910 (2018).
 39. Vial, S., Pastoriza-Santos, I., Pérez-Juste, J. & Liz-Marzán, L. M. Plasmon coupling in layer-by-layer assembled gold nanorod films. *Langmuir* **23**, 4606–4611 (2007).
 40. Fink, G. *et al.* The mitotic kinesin-14 Ncd drives directional microtubule-microtubule sliding. *Nat. Cell Biol.* **11**, 717–723 (2009).
 41. Tinevez, J. Y. *et al.* TrackMate: An open and extensible platform for single-particle tracking. *Methods* **115**, 80–90 (2017).

Figures

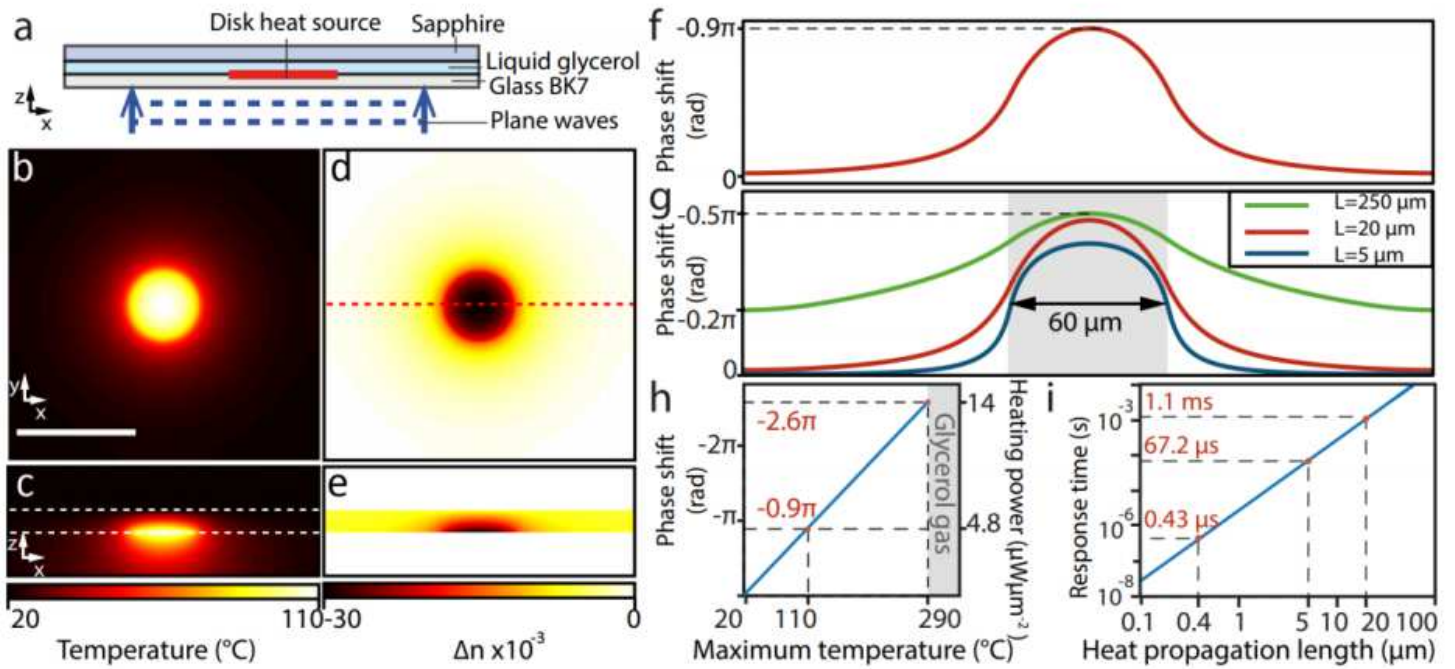


Figure 1

Numerical simulation of the spatial phase modulator. a) Illustration of the structure used. b) 2D map of temperature in the xy cross-section and c) xz cross-section (scale bar=100 μm). The boundaries of the thermo-optic material are indicated by the two white dashed lines. d) Resulting refractive index variation in the xy cross-section, and e) in the xz cross-section. f) Phase-shift profile of a plane wave propagating through the structure in z at the position of the red dashed line in d). g) Phase-shift profiles for different thicknesses of the thermo-optic layer. Heating powers of 0.4 $\mu\text{W}\mu\text{m}^{-2}$, 2.6 $\mu\text{W}\mu\text{m}^{-2}$, and 14 $\mu\text{W}\mu\text{m}^{-2}$ were considered for thicknesses of 250 μm , 20 μm , and 5 μm respectively. h) Peak phase-shift and corresponding heating power as a function of the peak temperature change (glycerol thickness=20 μm). i) Response time of the temperature change as a function of the characteristic dimension according to the model.

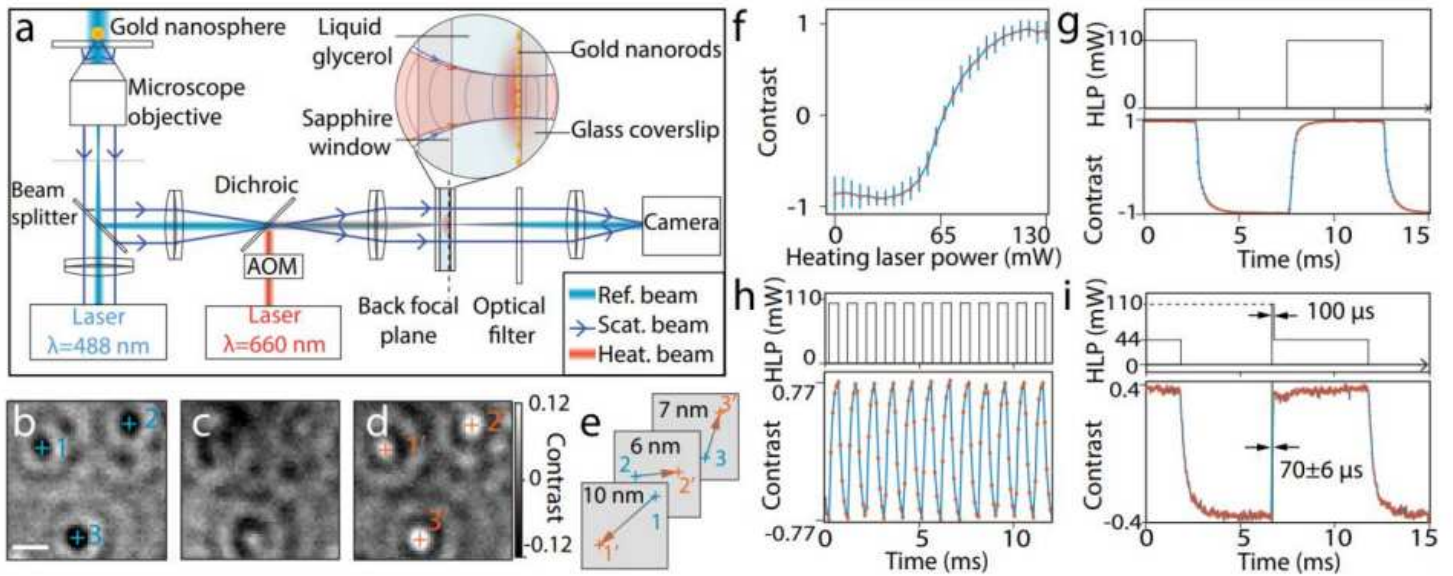


Figure 2

Experimental characterization of the PT-SLM. a) Layout of the setup (not to scale), details of the phase modulator structure are magnified. b-d) Normalized iSCAT images of 30-nm single gold nanospheres at heating laser powers P_{heat} (total power incident on the modulator structure) of b) 0 mW, c) 65 mW, d) 110 mW. (Scale bar=500 nm). Blue and orange crosses and numbers indicate the positions used to assess the lateral distortion. e) Change in the fitted position of the three nanoparticles indicated in b) and d). f) Calibration curve of the particle contrast dependence on the heating power. Error bars indicate the standard deviation of the experiment. g) Time series of the contrast of a gold nanosphere modulated with a rectangular signal at 100 Hz (HLP = Heating Laser Power) and h) at 1 kHz. i) Contrast time series for an arbitrary-shaped heating modulation. The upper diagram shows the corresponding temporal profile of the heating beam intensity.

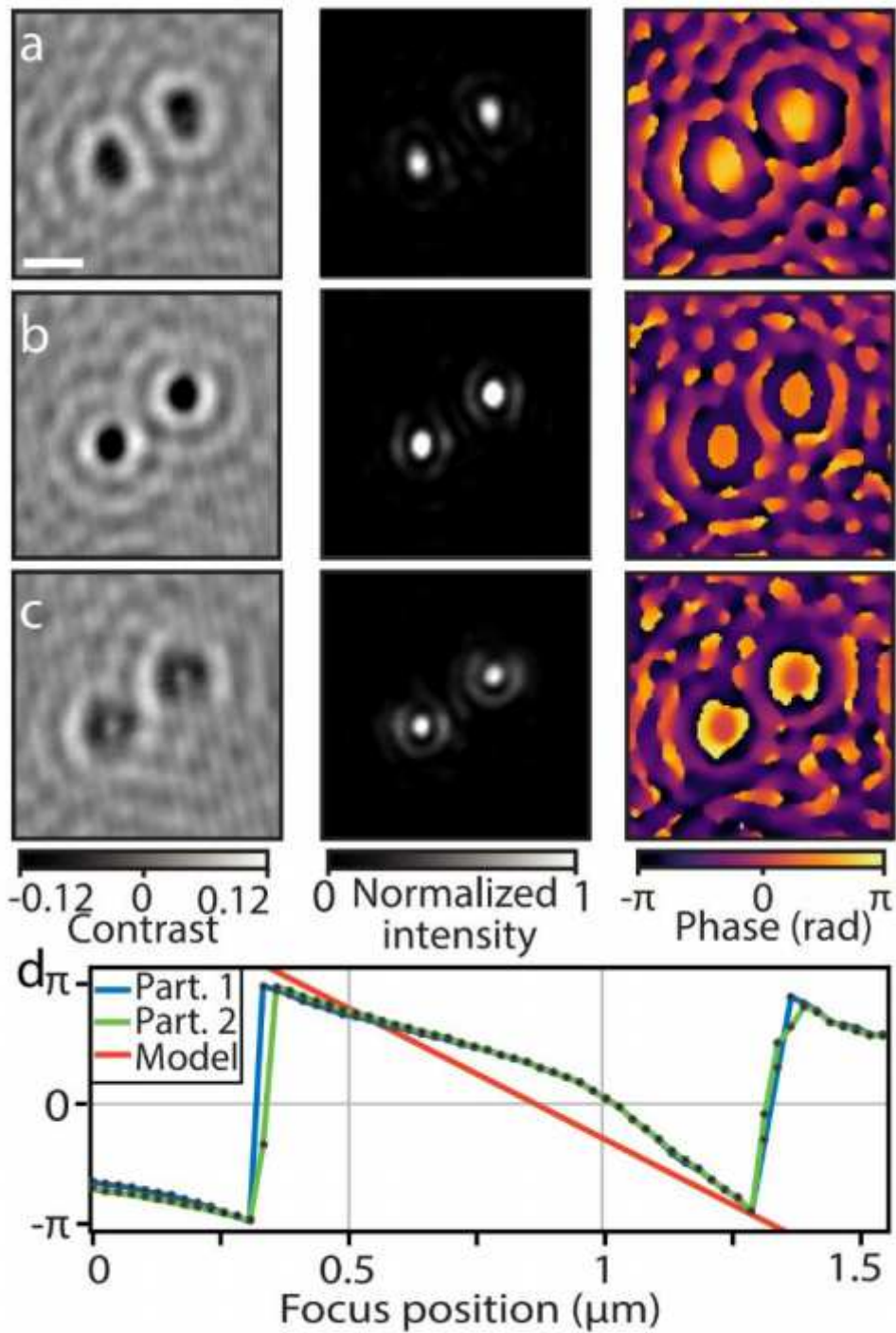


Figure 3

Quantitative phase imaging of gold nanoparticles. a-c) From left to right: iSCAT contrast, reconstructed intensity, and phase image of two gold nanoparticles at the focus positions: a) 0.35 μm , b) 0.6 μm and c) 0.85 μm . Scale bar 500 nm. d) Focus position dependence of the phase for the two particles shown in a-c). A theoretical prediction is shown in red.

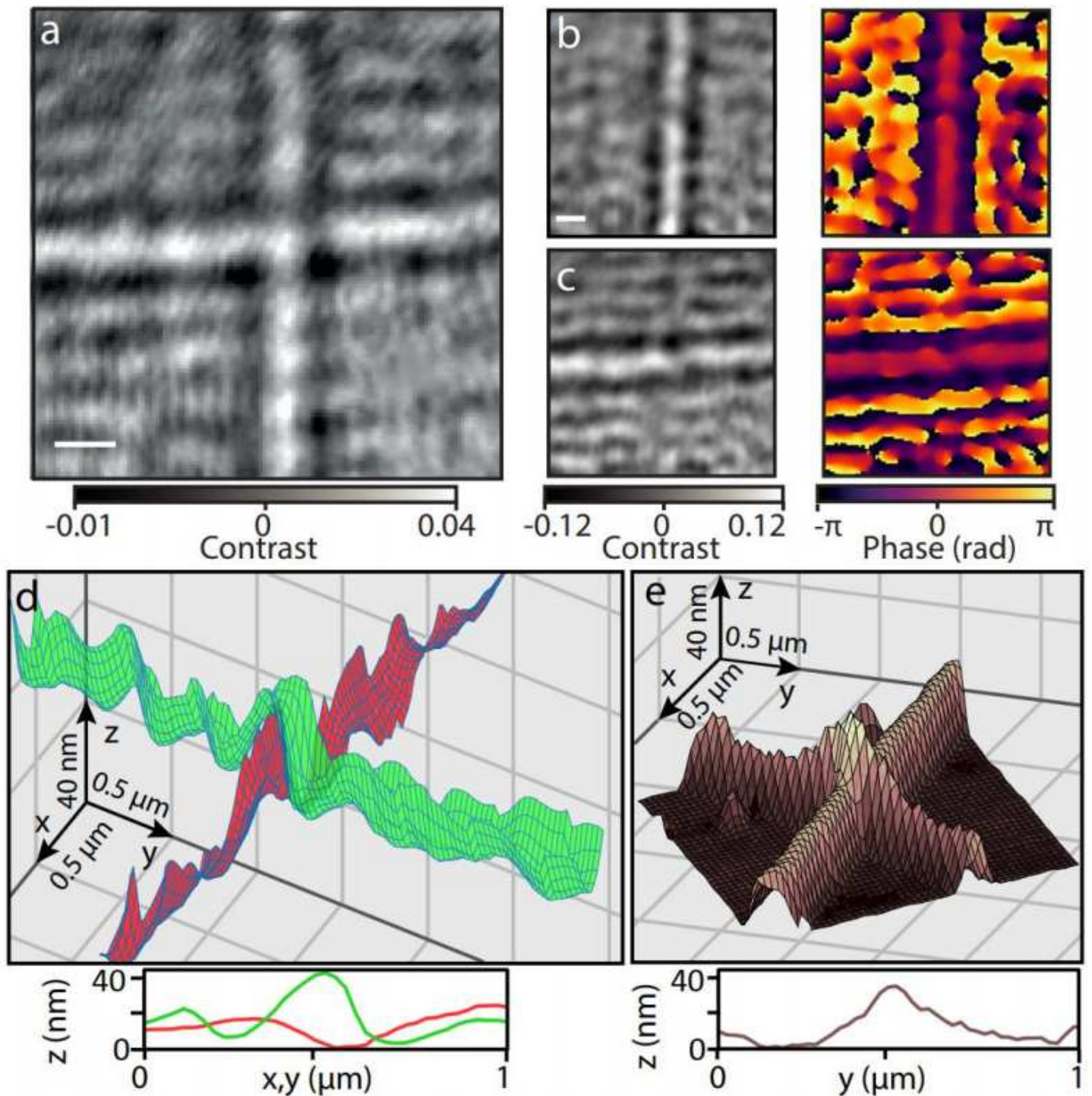


Figure 4

Quantitative phase imaging of microtubules. a) iSCAT image of two microtubules. Scale bar 500 nm. b-c) Separated iSCAT images and phase images of individual microtubules shown in a). d) 3D reconstruction of the crossing microtubules and the cross-section height profile. e) AFM image of microtubule crossing and the corresponding height profile.

Supplementary Files

This is a list of supplementary files associated with this preprint. Click to download.

- [SupplementaryInformationFastphotothermalspatiallightmodulation.pdf](#)